LANGMUIR

pubs.acs.org/Langmuir

Article

Fabrication of Bi_2O_3/Bismuth Titanates Modified with Metal−Organic Framework-In_2S_3/$CdIn_2S_4$ Materials for Electrocatalytic H_2 Production and Its Photoactivity

Krishnakumar Balu,*,¶ Balakrishna Avula, Mani Durai,¶ Sakthivel Kumaravel, Ernesto Chicardi,* Ranier Sepúlveda, Elangovan Erusappan, Imran Hasan, and Young-Ho Ahn*

Cite This: *Langmuir* 2023, 39, 15055−15066

Read Online

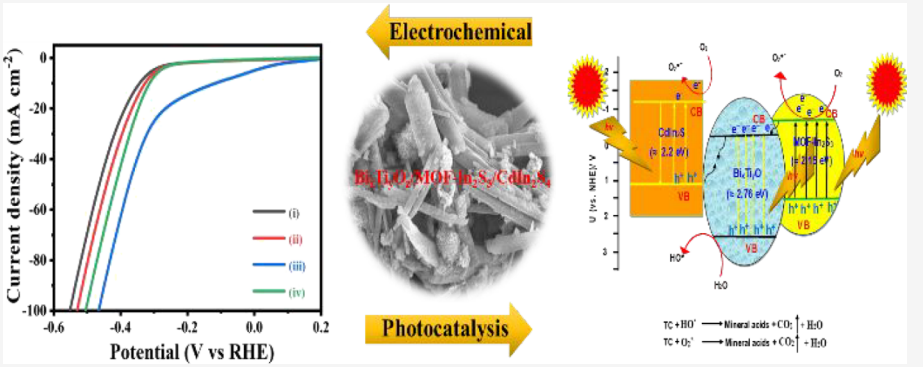

ABSTRACT: Compositional and structural elucidation of the materials is important to know their properties, chemical stability, and electro-photoactivity. The heterojunction electrocatalyst and photocatalyst activity could open a new window for solving the most urgent environmental and energy problems. Here, for the first time, we have designed and fabricated Bi_2O_3/bismuth titanates modified with MOF-In_2S_3/$CdIn_2S_4$ materials by a stepwise process. The detailed structural elucidation and formation of mixed composite phases were studied in detail. It has been found that the formed composite was efficiently utilized for the electrocatalytic H_2 production reaction and the photocatalytic degradation of tetracycline. XRD patterns for the metal−organic framework-In_2S_3 showed a main compound of MOF, and it was assigned to a MIL-53 MOF phase, with a monoclinic structure. The addition of $CdCl_2$ onto the MOF-In_2S_3 phase effectively produced a $CdIn_2S_4$ flower platform on the MOF rods. The uniform dispersion of the bismuth titanates in MOF-In_2S_3/$CdIn_2S_4$ materials is detected by mapping of elements obtained by dark-field HAADF-STEM. Finally, the predictions of how to integrate experiments and obtain structural results more effectively and their common development in new heterojunctions for electro-/photocatalytic applications are presented.

INTRODUCTION

Currently, global energy production is majorly dependent on fossil fuels. Industrialization energy needs to scale up as a function of population growth; it has been expected that the current energy demand will be increased three times in the next few decades, and more clean energy sources such as hydrogen need to be used. To date, a large number of composite materials have been reported for efficient hydrogen evolution and harmful compound degradation.[1−12] However, from the application point of view, it is still difficult to utilize these materials for efficient production of H_2 using direct solar light due to the wide band gap (>3 eV), being only active under high energy UV light. Bi_2O_3-based materials are potential electrocatalytic materials with high conductivity and low melting points.[13,14] Therefore, at the beginning of the 21st century, researchers focused on bismuth-based materials for energy and environmental-related applications.[15−17]

Due to the close relationship between the above constraints and their active characteristics, the adjustment of size, shape, and crystal structure is essentially dynamic.[18−22] The practical applications in several fields make the synthesis of modified binary and ternary chalcogenide compounds by various methods extremely interesting for research. Due to their distinct optoelectronic, electronic, optical, and catalytic capabilities, metal sulfides and chalcogenides (ternary, AB_2S_4; A = M^{2+}, B = M^{3+}) have been the focus of significant research

Received: July 18, 2023
Revised: September 28, 2023
Published: October 16, 2023

for several years.[23−27] Due to its intriguing applications in the disciplines of optics, photoconductivity, and optoelectronics, In_2S_3, a binary chalcogenide, has garnered special attention. Its high photoconductivity, chemical stability, and low-dimensional or nanoscale size made In_2S_3 a promising material for redox catalysts.[28−30] It also has good electron transport properties and slow charge recombination, which make it a suitable catalyst for photo- and electrocatalytic applications.

Sheng-qi Guo et al.[31] developed a self-assembly method for the hydrothermal production of In_2S_3 nanotubes along with rGO. The process is performed through the use of $InCl_3$, thioacetamide, and GO as precursors and poly(vinyl alcohol) (PVA) as a template in a water medium. The authors claimed that the sulfur source and template are important parameters for directing the structure and morphology of the produced In_2S_3. The formed composite was effectively utilized for electrocatalytic iodide species reduction reaction. Efficient photoelectrochemical (PEC) water splitting via Zr-doped In_2S_3 2D nanoflakes was reported by Ligang Wang et al.[32] The nanoflakes were obtained by reaction between $In(NO_3)_3.4H_2O$ and thioacetamide in an octanol/octylamine mixture via a hydrothermal approach. The Zr-modified In_2S_3 has relatively negative conduction band edges and favors the visible light absorbance tendency via the comfortable band gap energies.

Because of their numerous industrial applications, AB_2S_4-type semiconductors with layered structures have gained some attention. Recently, Xi Chen et al.[33] created a globular flower-like $CuS/CdIn_2S_4/ZnIn_2S_4$ and successfully used it for hydrogen evaluation and harmful pollutant degradation processes. The composite material was synthesized using nitrate salts of metal ion (Cu, Cd, In, and Zn) precursors with thioacetamide by a microwave-assisted hydrothermal reaction. The surface morphology of the produced composite was globular and flower-like, which contributed significantly to its high surface area and catalytic activity. Metal−organic frameworks (MOFs) have received a lot of interest recently because of their adaptable structural design, significant specific surface area, and high porosity.[34] MOF-based $CdIn_2S_4$ ($CdIn_2S_4$@NH_2-MIL-125) was synthesized via the hydrothermal method.[34] Authors claimed that the efficient production of hydrogen by the composite may be due to the formation of a heterojunction of NH_2-MIL-125 with $CdIn_2S_4$.

Even pristine or unmodified bismuth oxides have good catalytic properties. Bismuth-based nanocomposites have incredible applications in wastewater treatment and electrochemical and energy production.[35−39] There are many bismuth-based composites available in the literature; out of the reported developed materials, the bismuth titanates have been shown as efficient base materials for energy and environmental applications. Ning Zhang[40] reported that the photocatalytic activity of $Bi_4Ti_3O_{12}$ increased when modified with CuS. The combination of these materials was obtained by hydrothermal synthesis. The modified composite showed potential degradation activity against Rhodamine B (Rh B) dye. Another bismuth titanate-based material $Bi_{12}TiO_{20}$ modified with hydrochar and BiOBr was reported by Yulan Ren.[41] The formed $HC/BiOBr/Bi_{12}TiO_{20}$ microsphere is efficiently utilized for pollutant degradation. Here, we report the formation of the bismuth oxide/bismuth titanate phase modified with MOF/In_2S_3. The addition of cadmium ions produced $CdIn_2S_4$ via an ion-exchange reaction on the surface of MOF/In_2S_3. The structural and morphological properties and the combination of the composite materials were studied in detail. The combination of bismuth titanates with MOF-$In_2S_4/CdIn_2S_4$ is effectively utilized for electrocatalytic "H_2" evaluation reactions. In addition, the photocatalytic activity against tetracycline (TC) degradation under solar light has been studied.

MATERIALS AND METHODS

Chemicals Used for This Study. Cadmium Chloride ($CdCl_2$·$5H_2O$), indium nitrate $In(NO_3)_3$·XH_2O, bismuth nitrate ($Bi(NO_3)_3$·$5H_2O$) pentahydrate, 1,4 benzene carboxylic acid, titanium isopropoxide, antibiotic TC, thiourea, dimethylformamide (DMF), benzyl alcohol, bought from Sigma-Aldrich, served as the basis for creating the bismuth oxide/bismuth titanates/MOF-$In_2S_4/CdIn_2S_4$ composites.

Instrumentations. The crystallinity and the structural properties of the MOF-In_2S_4, MOF-$In_2S_4/CdIn_2S_4$, and bismuth titanates have been determined by powder X-ray diffraction patterns utilizing the Miniflex, Rigaku, Japan, PXRD [nickel filter CuKα radiation (30 kV, = 1.5419; range of 10−80)] system. The visible absorbance and band gap of the synthesized materials were obtained by a Neosys-2000 instrument (UV-DRS, in the range between 200 and 800 nm). The photoluminescent measurements were made with a Scinco (Korea) model spectrofluorometer. The surface morphology of the materials was obtained (10 kV- accelerating voltage) by a Hitachi S-4800 instrument (FE-SEM). On a Si-wafer substrate, the samples were coated. With a 120 kV operating accelerating voltage, the FEI-Tecnai TF-20 transmission electron microscope was used to create TEM/FE-TEM pictures and selected area electron diffraction (SAED) patterns. Before the tests were performed, the samples were dispersed in ethanol and put onto copper grids coated with carbon. With the use of K-Alpha from Thermo Scientific, XPS spectra were obtained. The main excitation was the nonmonochromatic Al K line at 180−200 W. Using Micromeritics ASAP 2000 and nitrogen adsorption at 77 K, the specific surface areas of the materials were calculated using the BET equation.

Synthesis of Bismuth Titanates ($Bi_xTi_yO_z$). About 3.64 g (7.5×10^{-3} M) of bismuth nitrate pentahydrate was dissolved in 15 mL of benzyl alcohol and stirred for 15 min. To this was added 15 mL of benzyl alcoholic solution containing 0.186 g (0.646×10^{-3} M) of titanium isopropoxide. The stirring was continued for 4 h. After that, the mixture was transferred into a 50 mL of stainless-steel Teflon autoclave and kept at 130 °C for 24 h. The final precipitate was obtained after three washings with a (1:1) EtOH:H_2O solution, 48 h of drying at 80 °C, and 3 h of calcination in a muffle furnace at 450 °C.

MIL- 53 (In) Prism (MOF). A 20 mL solution of DMF containing 1100 mg of 1,4-benzene carboxylic acid (Terephthalic acid) was added, while stirring, to the 900 mg of indium nitrate that had been dissolved in the 20 mL of DMF. The mixture was then reflexed for 30 min at 120 °C. Three EtOH washes were performed on the precipitate that had developed (MOF).

Synthesis of In_2S_3 from the MIL- 53 Indium Precursor (MOF-In_2S_3). The obtained MIL- 53 prism was added into 40 mL of an ethanolic solution containing 685 mg of thiourea under stirring conditions, and stirring continued further for 15 min. It was then put into a 50 mL Teflon-coated stainless-steel autoclave and kept at 180 °C for 3h. The formed precipitate (MOF-In_2S_3) was washed three times with the mixture of (1:1) EtOH:H_2O and dried at 60 °C for 5 h.

Synthesis of MOF-$In_2S_3/CdIn_2S_4$. About 0.8145 g of MOF-In_2S_3 (0.0025 M with respect to In_2S_4) was dispersed in 20 mL of water, then 20 mL of an aqueous solution containing 0.2854 g of (0.0012 M) $CdCl_2$ was added while stirring at 60 °C, and then, stirring was continued further 10 min; after that, the formed precipitate was washed with ethanol and dried in at 80 °C for 24 h in order to obtained MOF-$In_2S_3/CdIn_2S_4$.

Synthesis of $Bi_xTi_yO_z$/MOF-$In_2S_3/CdIn_2S_4$ and $Bi_xTi_yO_z$/MOF-In_2S_3. For $Bi_xTi_yO_z$/MOF-$In_2S_3/CdIn_2S_4$, about 750 mg of $Bi_xTi_yO_z$ was dispersed in 25 mL of the 1:1 EtOH/water mixture. To this was

https://doi.org/10.1021/acs.langmuir.3c02031
Langmuir 2023, 39, 15055−15066

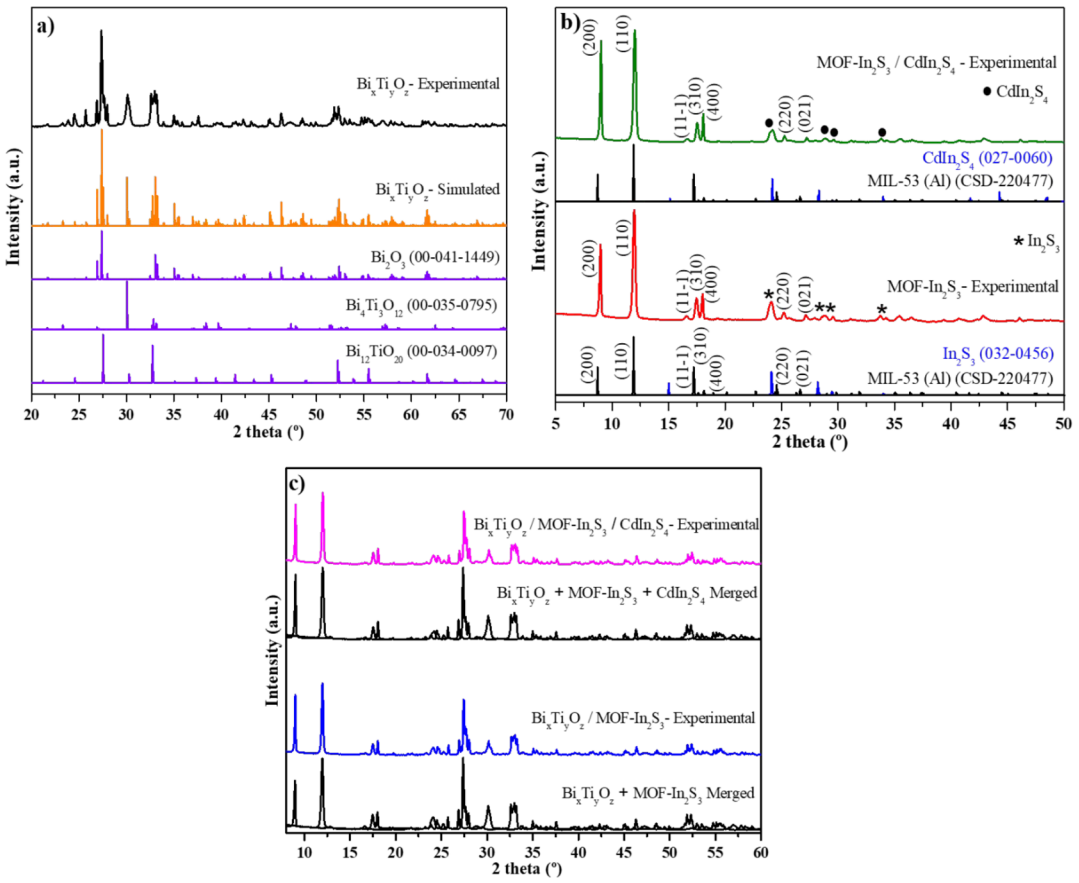

Figure 1. X-ray diffractograms for (a) $Bi_xTi_yO_z$ material (black) and the simulated XRD pattern (orange) from the indexed phases (blue); (b) MOF-In_2S_3 and MOF-In_2S_3/$CdIn_2S_4$ materials (red and green, respectively) together with the simulated XRDs for indexed phases (black and blue diffractograms); (c) $Bi_xTi_yO_z$ /MOF-In_2S_3 and $Bi_xTi_yO_z$ /MOF-In_2S_3/$CdIn_2S_4$ materials. Merged diffractograms from the experimentally synthesized materials are also displayed for comparison purposes.

added 25 mL of solution containing 250 mg of MOF-In_2S_3/$CdIn_2S_4$ dispersion. The stirring continued for 5h. The mixture was then filtered, and ethanol was washed and dried at 80 °C for 24 h. For comparison purposes, the composite $Bi_xTi_yO_z$/MOF-In_2S_3 was prepared with the same procedure with the respective amount of MOF-In_2S_4.

Electrocatalytic Water Splitting Experiment. Linear sweep voltammetry (LSV) and cyclic voltammogram (CV) measurements were used to evaluate the H_2 evaluation activity of the produced materials. The working electrodes were prepared by the following method. The samples were coated on nickel form (NiF) support (1 cm × 1 cm). About 10 mg of the samples was mixed with 10% polyvinylidene fluoride and 10% activated carbon in *N*-methyl-2-pyrrolidone. The sample-coated nickel form was dried at 50 °C overnight. Calomel electrodes (Hg/HgO electrodes) and platinum electrodes served as the counter and reference electrodes, respectively. The stable overlap curves were confirmed by multiple scanning CV obtained by 1 M KOH solution. The Tafel slopes were obtained using the LSV curve, and the overlap potential was set at 10 mA cm^{-2}. The stability of the $Bi_xTi_yO_z$/MOF-In_2S_3/$CdIn_2S_4$/NiF electrode was confirmed by a chronopotentiometry study. For electrocatalytic water splitting, the IVIUM instrument was used.

Photocatalytic Degradation Experiments under Solar Light. The produced materials' photocatalytic abilities to degrade TC were assessed in direct sunlight (95 mW/cm^2). The solar experiments were carried out in Gyeongsan, South Korea, between 11 a.m. and 2 p.m. The solar light intensity was nearly constant during the studies. In each experiment, 100 mL of 20 ppm TC solution was mixed with a measured quantity (20 mg/100 mL) of the synthesized materials in a beaker, and the dark reaction was performed under dark conditions for 1 h; in order to obtain the adsorption capability of the materials, after reaching the equilibrium, the catalyst containing solution was irradiated under direct sunlight. The samples (3−4 mL) were taken at predetermined intervals, centrifuged, and examined with a UV−vis spectrometer, and the analytical wavelength of TC was 357 nm.

RESULTS AND DISCUSSION

XRD Analysis. The experimental XRD spectra for $Bi_xTi_yO_z$, MOF-In_2S_3, $Bi_xTi_yO_z$/MOF-In_2S_3, $Bi_xTi_yO_z$/MOF-In_2S_3/$CdIn_2S_4$, and MOF-In_2S_3/$CdIn_2S_4$ specimens are shown in Figure 1. Concretely, for the specimen $Bi_xTi_yO_z$ (Bi−Ti−O photocatalyst), the corresponding experimental XRD pattern (Figure 1a) showed the presence of a majority phase, bismuth oxide (Bi_2O_3), with a monoclinic structure and *P*21/*c* space group symmetry (SGS, ref no. 00-041-1449 in the PDF4 + ICDD database). Another two important phases could be also indexed: concretely, two different bismuth titanates. They are $Bi_{12}TiO_{20}$ (ref no. 00-034-0097, cubic structure, *I*23 SGS, in th- PDF4 + ICDD database) and $Bi_4Ti_3O_{12}$ (ref no. 00-035-0795, orthorhombic structure, *Cmmm* SGS, in the PDF4 + ICDD database). The simulated XRD pattern from the three phases indexed (orange XRD in Figure 1a) matched with the experimental XRD, corroborating that these phases formed.

On the other hand, the specimen MOF-In_2S_3, corresponding to the experimental XRD pattern for the metal−organic framwork-In_2S_3 photocatalyst system (Figure 1b), showed a main compound that was assigned to a MIL-53 MOF phase, with a monoclinic structure and *Cc* SGS, according to

https://doi.org/10.1021/acs.langmuir.3c02031
Langmuir 2023, 39, 15055−15066

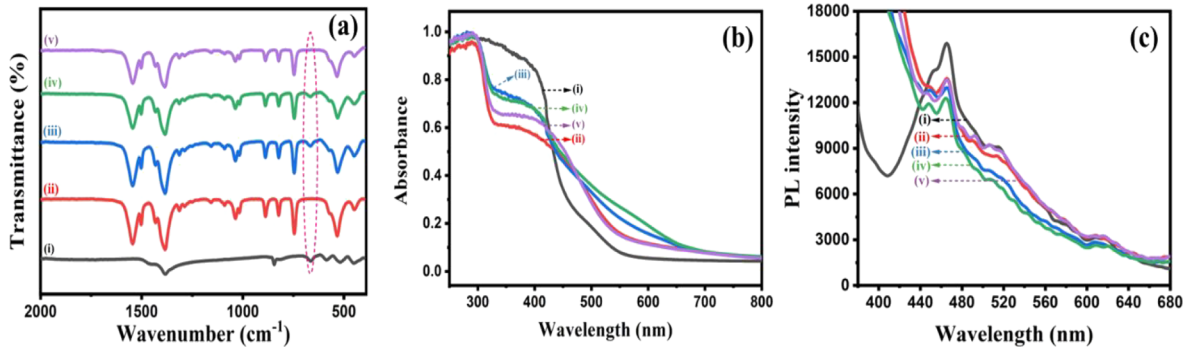

Figure 2. (a) FT-IR, (b) DRS, and (c) PL spectra of synthesized materials (i) $Bi_xTi_yO_z$, (ii) MOF-In_2S_3, (iii) $Bi_xTi_yO_z$/MOF-In_2S_3, (iv) $Bi_xTi_yO_z$/MOF-In_2S_3/$CdIn_2S_4$, and (v) MOF-In_2S_3/$CdIn_2S_4$.

reference no. 220477 found in the Cambridge Structural Database (CSD).

There, the cationic metallic element in the MOF showed is Al^{3+}. However, for the MOF-In_2S_3 material, the metallic element corresponds to the In^{3+} cation. This aspect was caused due to the different cation radii tetracoordinate of Al^{3+} (0.39 Å) and In^{3+} (0.62 Å), a shift of peaks to lower 2 theta degree, as can be easily observed for the (200) and (110) crystallographic planes. Thus, MOF-53 (In) was correctly formed. Also, following the same CSD database, the indium sulfide (In_2S_3), with a cubic structure and $Fd\bar{3}m$ SGS (ref no 1596369 in the CSD database). Thus, no other phase could be detected in this MOF-In_2S_3 specimen, suggesting the successful formation of the MOF-In_2S_3 hybrid material.

Subsequently, the experimental XRD for the specimen with the addition of $CdCl_2$ salt in the MOF-In_2S_3 specimen, according to the procedure mentioned above in the experimental section, revealed the presence of the MOF-53 (In)-In_2S_3 hybrid material; there was no decomposition during the procedure of introduction of $CdCl_2$. In addition, another phase was indexed with the same structure and lattice parameter as the cubic In_2S_3. However, in this case, this phase corresponds to the ternary chalcogenide cadmium indium sulfide, $CdIn_2S_4$, according to the ref pattern no. 027-0060 of the PDF4 + -ICDD database (cubic structure and $Fd\bar{3}m$ SGS). As can be observed in the specimen labeled as MOF-In_2S_3/$CdIn_2S_4$ (see Figure 1b), this phase showed an analogous structure compared to indium sulfide.

Finally, in Figure 1c, the other two specimens developed are exposed, based on a combination of $Bi_xTi_yO_z$ and MOF-In_2S_3 (specimen $Bi_xTi_yO_z$/MOF-In_2S_3) and the mixture of $Bi_xTi_yO_z$ and MOF-In_2S_3/$CdIn_2S_4$ (specimen $Bi_xTi_yO_z$/MOF-In_2S_3/$CdIn_2S_4$). Thus, due to the procedure evolving only the suspension mixture in water, the phases formed are the summary of the existing phases of their reagents, as can be easily corroborated by attending to the analogous experimental XRD obtained by the merging of $Bi_xTi_yO_z$ with MOF-In_2S_3 and $Bi_xTi_yO_z$ with MOF-In_2S_3/$CdIn_2S_4$. Therefore, the indexed phases in $Bi_xTi_yO_z$/MOF-In_2S_3 are the above-mentioned $Bi_xTi_yO_z$ (Bi_2O_3, $Bi_4Ti_3O_{12}$, and $Bi_{12}TiO_{20}$) and MOF-53 (In)-In_2S_3 from MOF-In_2S_3. Analogously, the specimen $Bi_xTi_yO_z$/MOF-In_2S_3/$CdIn_2S_4$ (Figure 1c) presented the same phases in addition to $CdIn_2S_4$. All these assertions extracted by XRD are corroborated later by the TEM analysis.

Surface Functional Group Analysis and Optical Studies. The surface functional groups were analyzed by the IR technique, and the IR spectra of $Bi_xTi_yO_z$, MOF-In_2S_3, $Bi_xTi_yO_z$/MOF-In_2S_3, $Bi_xTi_yO_z$/MOF-In_2S_3/$CdIn_2S_4$, and MOF-In_2S_3/$CdIn_2S_4$ specimens are presented in Figure 2a. In $Bi_xTi_yO_z$ and its modified specimens, the common signal of oxygen−metal bonds is observed from 500 to 860 cm^{-1}. The two significant peaks at about 846 and 586 cm^{-1} were attributed to the stretching vibrations of Bi−O and Ti−O bonds, respectively. This confirms the formation of the $Bi_xTi_yO_z$ structure.[42] Moreover, in the $Bi_xTi_yO_z$ specimen, the strong bismuth titanate peak appeared at 657 cm^{-1}, and this peak remains unchanged in all $Bi_xTi_yO_z$-containing specimens (Figure 2a, highlighted part). The IR spectrum of MOF-In_2S_3 and MOF-based composites showed that two strong bands that appeared at 1386 and 1548 cm^{-1} are assigned to asymmetric and symmetric stretching vibrations of O═C−O group (from Terephthalic acid) from MIL-53 MOF.[43] The C═C groups in the benzene ring's characteristic vibration are represented by the tiny band at 1501 cm^{-1}, and C−H bending vibration is observed at 744 cm^{-1}.[44] The main characteristic absorption peak of In_2S_3 is observed at 1430 cm^{-1} for all MOF-In_2S_3 and MOF-loaded samples.[45] After $CdCl_2$ addition to MOF-In_2S_3, the IR spectrum of MOF-In_2S_3/$CdIn_2S_4$ almost resembles that of MOF-In_2S_3.

The light absorbance behavior of the prepared samples was measured via solid-state UV-DRS measurements, and the results are presented in Figure 2b. The DRS reveals that the Bi_xTi_yOz component has strong UV−vis absorbance until 430 nm, and after that, the absorbance intensity decreased in the entire visible region. The absorbance of MOF-In_2S_3 increased from 450 nm to the entire visible region (blue, 445−500 nm; green, 500−545 nm; 545- 580 nm, orange, 580−600 nm, and red-600−750 nm). The combination of these two composites shows a higher absorbance in the visible region from blue to red (445−750 nm); in particular, the visible absorbance of the $Bi_xTi_yO_z$/MOF-In_2S_3/$CdIn_2S_4$ component increased in the entire visible region when compared with other components. After the addition of $CdCl_2$ into $Bi_xTi_yO_z$/MOF-In_2S_3, the absorbance intensity of $Bi_xTi_yO_z$/MOF-In_2S_3 increased from mid of blue to (480 nm) to red (750 nm) region; this may be the formation of $CdIn_2S_4$ phase, that is, $Bi_xTi_yO_z$/MOF-In_2S_3/$CdIn_2S_4$. The formed heterostructure ($Bi_xTi_yO_z$/MOF-In_2S_3/$CdIn_2S_4$) efficiently degrades the TC under direct solar light (discussion comes later) and effectively produced H_2 from water (discussion comes later). This study clearly revealed that there was a close interaction observed between $Bi_xTi_yO_z$ and MOF-In_2S_3, and $CdIn_2S_4$ components in $Bi_xTi_yO_z$/MOF-In_2S_3/$CdIn_2S_4$. After the addition of $CdCl_2$ in the MOF-

https://doi.org/10.1021/acs.langmuir.3c02031
Langmuir 2023, 39, 15055−15066

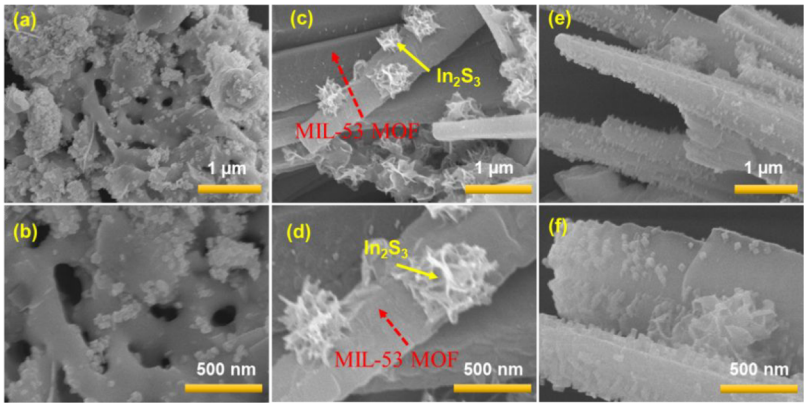

Figure 3. FE-SEM images of $Bi_xTi_yO_z$ (a and b), MOF-In_2S_3 (c and d), and $Bi_xTi_yO_z$/MOF-In_2S_3/$CdIn_2S_4$ (e and f).

In_2S_3, the formation of a new phased occurred on the surface of MOF-In_2S_3 via the ion-exchange reaction and could absorb the light over a wide spectrum of solar light (from blue to red region), which enhanced the visible light activity of the $Bi_xTi_yO_z$/MOF-In_2S_3/$CdIn_2S_4$ component.

Figure 2c represents the photoluminescent properties of the synthesized specimens. The intensity of the $Bi_xTi_yO_z$ specimen is higher than those of all of the synthesized materials. Generally, the higher PL intensity is caused by the fast e^-/h^+ recombination, which does not favor photocatalytic applications. However, the PL intensity of the $Bi_xTi_yO_z$/MOF-In_2S_3/$CdIn_2S_4$ specimen is low compared with other components. The $Bi_xTi_yO_z$ specimen has the PL emission at 464 nm, and the other $Bi_xTi_yO_z$-based specimens have the same PL emission, but the intensities of the emissions are less when compared with the $Bi_xTi_yO_z$ specimen. It may be due to the suppression of e^-/h^+ recombination, which favors the photocatalytic applications.

Surface Morphology Analysis by FE-SEM, TEM, and Elemental Mapping Studies. Surface morphology of the synthesized materials initially observed by field emission scanning electron microscopy (FE-SEM) and FE-SEM images of $Bi_xTi_yO_z$, MOF-In_2S_3, and $Bi_xTi_yO_z$/MOF-In_2S_3/$CdIn_2S_4$ are shown in Figures 3 and S1 (see Supporting Information). $Bi_xTi_yO_z$ has two different phases, well-separated round-shaped particles and shapeless layered structured particles (Figures 3a,b and S1a). In the same way, MOF-In_2S_3 also has two phases rod-like MIL-53 MOF and flower-like In_2S_3 (Figures 3c,d and S1b,c). The combination of these two particles produced $Bi_xTi_yO_z$/MOF-In_2S_3 (Figure S2a–c). The addition of Cd ion into this mixture produced $Bi_xTi_yO_z$/MOF-In_2S_3/$CdIn_2S_4$ (Figure 3e,f) and shows the individual $Bi_xTi_yO_z$ and MOF-In_2S_3 particles along with numerous small particles on the surface of MOF. This has been confirmed with MOF-In_2S_3/$CdIn_2S_4$ images (Figure S2d–f). The morphology and composition of the mixture in the composites were further analyzed by HR-TEM and elemental mapping analysis, and the results are discussed in detail.

The TEM study was carried out on the $Bi_xTi_yO_z$/MOF-In_2S_3/$CdIn_2S_4$ specimen, and the corresponding images with various locations and magnifications are shown in Figure 4. This specimen has been selected to corroborate the indexed phases formed because it is the most complex specimen, formed by the mixture of the specimens $Bi_xTi_yO_z$ and MOF-In_2S_3/$CdIn_2S_4$. The particles detected in Figure 4 exhibit different and diverse morphologies. Concretely, it was

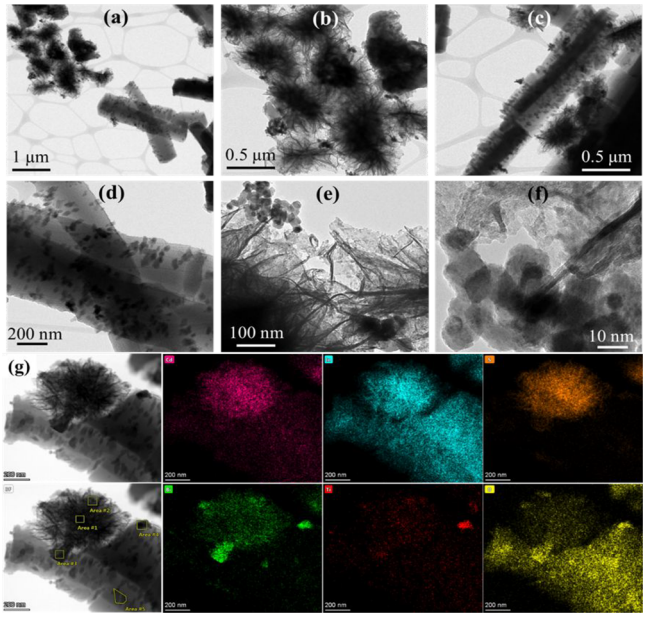

Figure 4. HR-TEM images (a–f) and the corresponding mapping (g) of the $Bi_xTi_yO_z$/MOF-In_2S_3/$CdIn_2S_4$ material. Colors in mapping: pink = Cd; light blue = In; orange = S; green = Bi; red = Ti; and yellow = O.

observed the typical irregular flower-type architectures were widely reported for the $CdIn_2S_4$.[46−48]

The architecture is, in fact, agglomerated with nanoparticles, as can be observed in Figure 4f. This morphology is not a strange structure. These irregular flower-type architectures are also commonly used for other complex sulfides like $ZnIn_2S_4$[49,50] and, even, for cubic β-In_2S_3[51,52] synthesized in the specimen MOF-In_2S_3, as the reagent to obtain the $Bi_xTi_yO_z$/MOF-In_2S_3/$CdIn_2S_4$ specimen. In addition, mapping XEDS carried out on different flower types of $CdIn_2S_4$ particles (areas 1 and 2 in Figure 4g, areas 2 and 3 in Figure S3, and area 1 in Figure S4) corroborated the presence of Cn, In, and S in them. Thus, the punctual semiquantitative XEDS composition gave the average composition displayed in Table 1, according to the $CdIn_2S_4$ stoichiometry.

In Figure 4, the other particles with different morphologies revealed submicrometric rods that are acting as hosts for embedded nanoparticles. By the analogous mapping XEDS study carried out for the flower-type $CdIn_2S_4$, it was observed that these rods are mainly composed of In and O, suggesting

https://doi.org/10.1021/acs.langmuir.3c02031
Langmuir 2023, 39, 15055−15066

Table 1. Punctual Semiquantitative XEDS Composition of the $Bi_xTi_yO_z$/MOF-In_2S_3/$CdIn_2S_4$ Specimen

	elements					
phase	Bi	Cd	In	O	S	Ti
$CdIn_2S_4$		11.2 ± 1.9	30.9 ± 2.1		58.0 ± 0.9	
MOF-53 (In)			19.5 ± 2.0	71.5 ± 2.0		
In_2O_3			36.5 ± 1.5	63.5 ± 1.5		
Bi−Ti−O	17.9 ± 2.8			67.9 ± 2.6		14.2 ± 0.5
Bi_2O_3	67.2 ± 1.8			32.8 ± 2.2		-

that they are, in fact, the MOF-53 (In) indexed by XRD (see Figures 4g, S3, and S4). Also, the embedded nanoparticles showed higher In and O brightness in comparison to the rest of the rod. In addition, the embedded nanoparticles are composed of indium oxide (In_2O_3), as shown in the marked area 5 in Figure 4g, which was not previously detected by XRD due to its nanometric size and low amount, due to which it can be masked by the rest of phases. Then, the submicrometer rods are formed, in fact, by In_2O_3@MOF-53. This type of hybrid material has been already developed by other systems like Au/MO*x*@MOF-5 (M = Zn, Ti; *x* = 1,2), Ru@MOF-5, and so forth.[53]

In addition, by HRTEM (Figure 5a) and the corresponding FFT (Figure 5b) images of those nanoparticles could be indexed, the interplanar distance of the (222) crystallographic planes (d = 0.29 nm) could be indexed, corroborating the In_2O_3 nature of those nanoparticles. However, the presence of In_2O_3 is interesting since the XRD for $Bi_xTi_yO_z$/MOF-In_2S_3 specimens used as mixing is formed by In_2S_3 instead of In_2O_3. Thus, the introduction of Cd in $Bi_xTi_yO_z$/MOF-In_2S_3/$CdIn_2S_4$ caused the transformation of some In_2S_3 by In_2O_3 because of the excess amount of S required, and the remaining excess In^{3+} cations react with oxygen to form nanoembedded particles of In_2O_3 into the MOF rods. To clarify this aspect, HRTEM images have been obtained also in the $Bi_xTi_yO_z$/MOF-In_2S_3 specimen. In Figure 5e−h, a high number of embedded nanoparticles could be clearly observed, corresponding undoubtfully to In_2S_3. The transformation of In_2S_3 in In_2O_3 did not take place due to the absence of Cd, which prevents the breakdown of In_2S_3. The indexation of the (400) and (440) interplanar distance from the embedded nanoparticles in the $Bi_xTi_yO_z$/MOF-In_2S_3 specimen corroborates this assertion (see Figure 5e−h). Finally, on the other hand, the isolated nanoparticles in the $Bi_xTi_yO_z$/MOF-In_2S_3/$CdIn_2S_4$ specimen (Figure 5c,d) are formed by the different bismuth titanates indexed by XRD, with the general formula of $Bi_xTi_yO_z$.

The third clear particle morphology is 0D nanoparticles and nanorods (clearly observed in Figure 4e,f, respectively. Attending to the XEDS mapping studies (Figure S3) these particles are composed of Bi, Ti, and O, suggesting they are the bismuth titanates determined by XRD. The composition exposed in Table 1 and determined from areas 1 and 4 in Figure S3 corroborated this assertion. However, the composition calculated did not match with the three bismuth compounds indexed by XRD, that is, the Bi_2O_3, the $Bi_{12}TiO_{20}$, and the $Bi_4Ti_3O_{12}$. This aspect suggests that these particles are in fact mixed nanoparticles of these three compounds. In this sense, regarding the Ti micrograph for Figure S3, it was detected some nanoparticles in the absence of Ti and the presence of Bi and O, corresponding to Bi_2O_3 (marked with a white circle).

The really nanosized groups of particles did not allow for carrying out accurate point EDS for each particle. Besides,

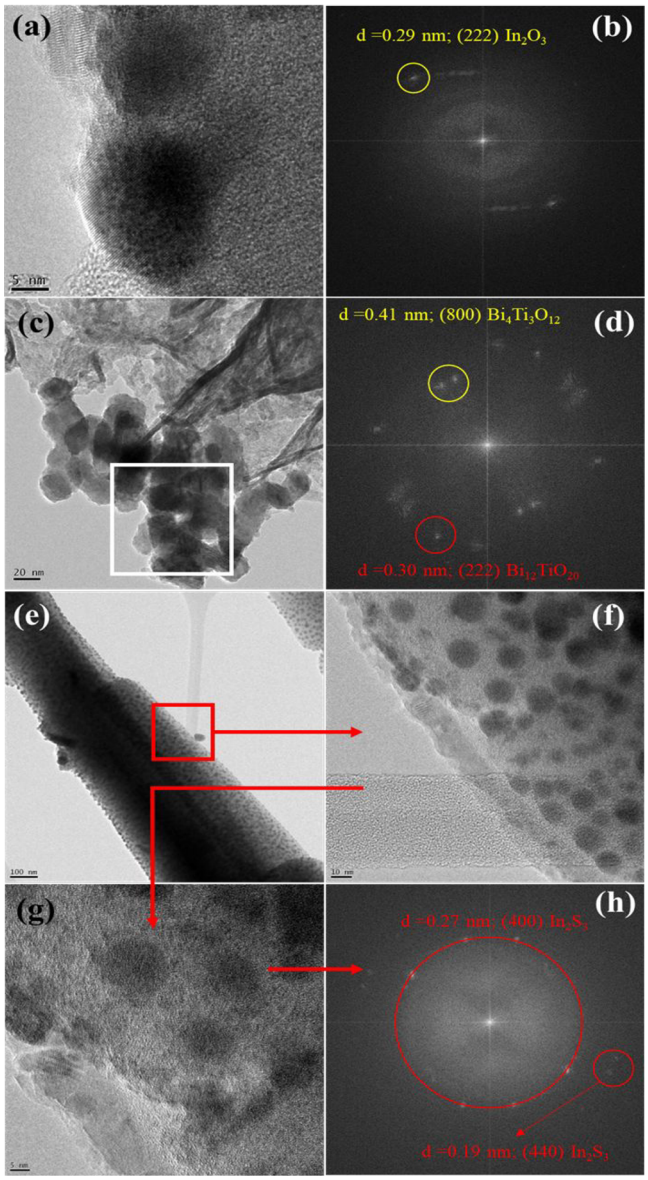

Figure 5. (a−d) HRTEM and FFT images for the $Bi_xTi_yO_z$/MOF-In_2S_3/$CdIn_2S_4$ material. The image (b) corresponds to the FFT image for the full HRTEM image displayed in (a). Image (d) shows the FFT for the white square marked in image (c); (e−h) HRTEM and FFT images for the $Bi_xTi_yO_z$/MOF-In_2S_3 material. The image (h) corresponds to the FFT image of the red square of image (g).

Bi_2O_3 was also detected as submicrometric particles, as can be observed in Figure 4g, in the zones marked as area 3 and area 4 in Figure S3. The EDS composition determined for those areas (see Table 1) now matched clearly with the Bi_2O_3 indexed previously by XRD. Finally, analogous to the submicrometric Bi_2O_3, submicrometric bismuth titanates were also found, as

https://doi.org/10.1021/acs.langmuir.3c02031
Langmuir 2023, 39, 15055−15066

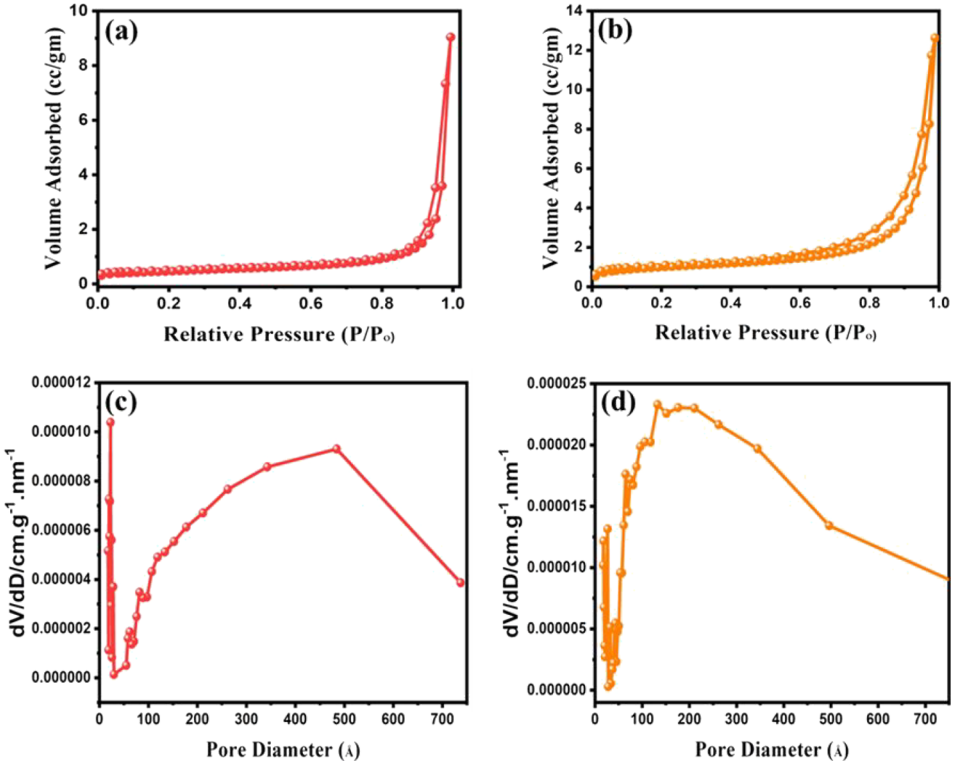

Figure 6. N_2 adsorption−desorption isotherms and pore size distribution of $Bi_xTi_yO_z$ (a and c) and $Bi_xTi_yO_z$/MOF-In_2S_3/$CdIn_2S_4$ (b and d).

can be corroborated in Figure S4 (marked with white circles). Due to interferences with the In_2O_3@MOF-53 rods, quantification by EDS was not determined.

BET Analysis. The surface area of bare $Bi_xTi_yO_z$ and $Bi_xTi_yO_z$/MOF-In_2S_3/$CdIn_2S_4$ was determined, and N_2 adsorption and desorption isotherms of $Bi_xTi_yO_z$ and $Bi_xTi_yO_z$/MOF-In_2S_3/$CdIn_2S_4$ are shown in Figure 6 together with pore size distribution. A type II hysteresis loop can be seen in the isotherms of $Bi_xTi_yO_z$ and $Bi_xTi_yO_z$/MOF-In_2S_3/$CdIn_2S_4$, and their corresponding BET surfaces, pore volumes, and average pore diameters are shown in Table S1. $Bi_xTi_yO_z$/MOF-In_2S_3/$CdIn_2S_4$ has a larger BET surface area (3.5302 m^2g^{-1}) than that of bare $Bi_xTi_yO_z$ (1.6171 m^2g^{-1}). Additionally, $Bi_xTi_yO_z$/MOF-In_2S_3/$CdIn_2S_4$ has a greater pore volume than pure $Bi_xTi_yO_z$.

XPS Analysis. The surface chemical states of sample $Bi_xTi_yO_z$/MOF-In_2S_3/$CdIn_2S_4$ were determined by XPS survey spectra, and high-resolution XPS spectra of Bi 4f, O 1s, In 3d, Cd 3d, Ti 2p, and S 2S are shown in Figure 7a−g, respectively. The survey spectrum (Figure 7a) corroborated the existence of Bi, O, In, Cd, Ti, and S elements in the composite. The Bi 4f spectrum (Figure 7b) showed binding energy peaks at 158.8 and 164.1 eV, which were attributed to the $4f_{7/2}$ and $4f_{5/2}$ signals having a splitting energy of 5.3 eV. According to the literature, these peaks suggest that Bi is in the 3^+ state.[54] The O 1s spectrum in Figure 7c showed two overlapped peaks at 529.5 and 533.7 eV. At a lower binning energy, the peak can be assigned to the metal−oxygen bonds in the bismuth oxide. However, the peak at 531.7 eV could be ascribed to the hydroxyl groups and organic compound present in the MOF.[55,56]

The In spectrum (Figure 7d) showed peaks at 445.1 ($3d_{5/2}$) and 452.6 ($3d_{3/2}$), which can be assigned to the In_2S_3 compound[57] with a splitting energy of 7.5 eV. The peak at 442.3 eV found after the peak deconvoluted was ascribed to the Bi $4d_{5/2}$ signal of the Bi−S bonds. Figure 7e showed the Cd spectrum with two main peaks at 405.0 ($3d_{5/2}$) and 411.8 ($3d_{3/2}$) having 6.8 eV of peak splitting energy, previously described in the literature for the $CdIn_2S_4$ compound.[58] In fact, $CdIn_2S_4$ peaks are located at lower binning energies due to the presence of Ti atoms.[59] The Spectrum of Ti 2p (Figure 7f) showed peaks at 457.7 and 465.9 eV, lower binding energy peak could correspond to Ti $2p_{3/2}$ at the Ti^{3+} state,[60] although some differences were found most likely due to the influence of Bi atoms in the existing $Bi_{12}TiO_{20}$ phase obtained by the XRD characterization. According to Dongfang Hou,[61] the peak at 465.9 eV can be caused by the overlapping of peaks Ti $2p_{1/2}$ and Bi $4d_{3/2}$ showing a broad bump to higher binding energies. However, due to the small amount of Ti atoms in the sample, the deconvolution peak processing analysis cannot be applied correctly. To identify the presence of sulfur, the S 2s spectrum was used due to the overlapping of the S 2p peaks with Bi 4f. The spectrum in Figure 7g showed a peak at 225.1 eV in agreement with the literature.[62]

H_2 Evaluation Activity. The electrochemical water splitting efficiency of the synthesized $Bi_xTi_yO_z$/MOF-In_2S_3/$CdIn_2S_4$/NiF electrodes along with those of MOF-In_2S_3/NiF, $Bi_xTi_yO_z$/MOF-In_2S_3/NiF, and MOF-In_2S_3/$CdIn_2S_4$/NiF electrodes was also evaluated in a 1 M KOH electrolyte solution using these electrodes with an electrochemical system (Figure 8). The $Bi_xTi_yO_z$/MOF-In_2S_3/$CdIn_2S_4$/NiF electrode has little significance when compared with MOF-In_2S_3/NiF, $Bi_xTi_yO_z$/MOF-In_2S_3/NiF, and MOF-In_2S_3/$CdIn_2S_4$/NiF electrodes, and the corresponding overpotentials are 82, 340, 325, and 309 mV, respectively, as shown in Figure 8a,b. Among the synthesized electrodes, the $Bi_xTi_yO_z$ /MOF-In_2S_3/$CdIn_2S_4$/NiF electrode has low overpotential (82 mV). As revealed by the overpotentials obtained at 10 mA cm^{-2}, the

https://doi.org/10.1021/acs.langmuir.3c02031
Langmuir 2023, 39, 15055−15066

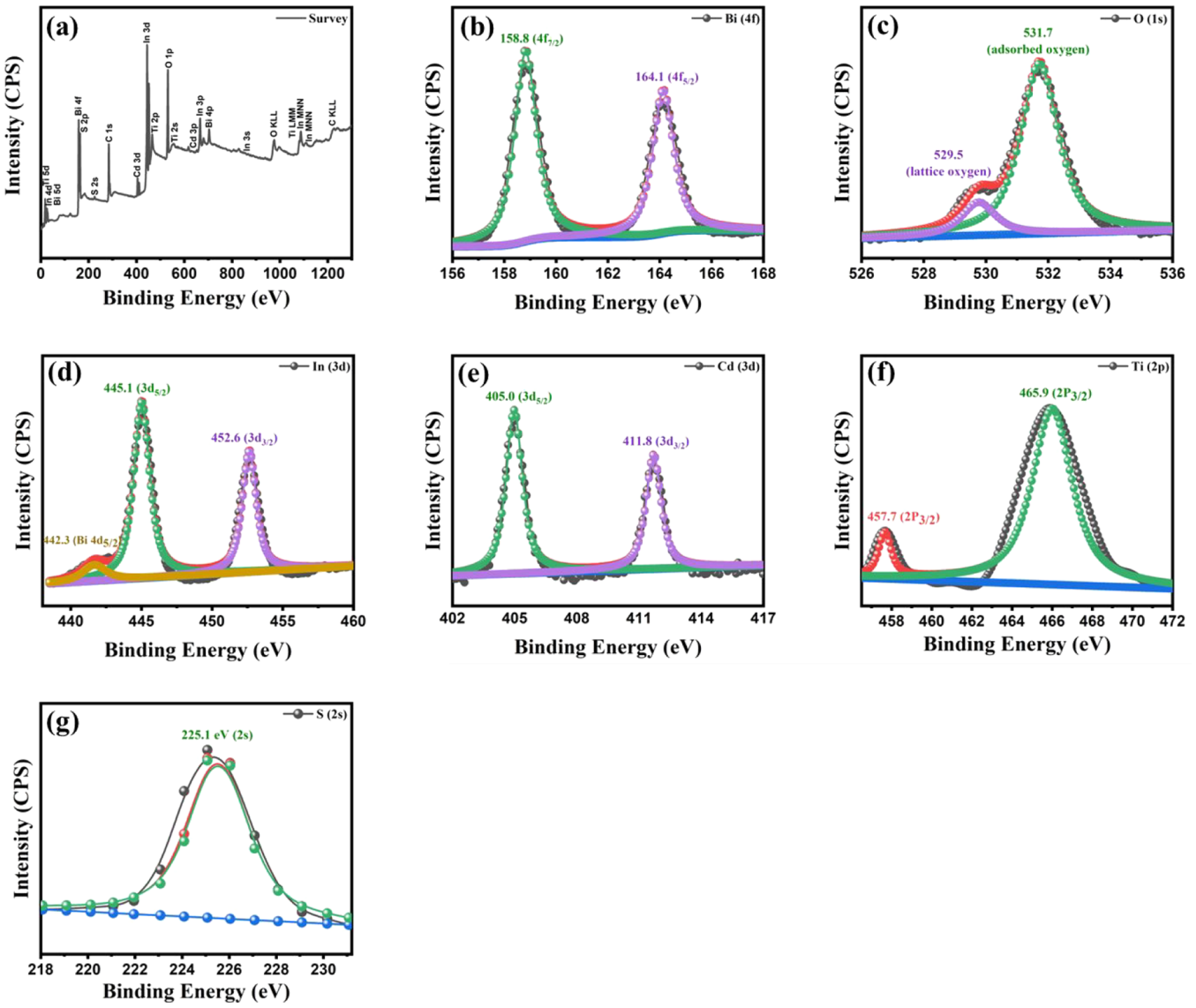

Figure 7. XPS of $Bi_xTi_yO_z$/MOF-In_2S_3/$CdIn_2S_4$, (a) survey spectrum, (b) Bi 4f, (c) O 1s, (d) In 3d, (e) Cd 3d, (f) Ti 2p, and (g) S 2s.

hydrogen evaluation reaction (HER) efficiency improved when $Bi_xTi_yO_z$ was incorporated into $CdIn_2S_4$/NiF. Moreover, the synergistic coupling effect of the electron transfer lowers the Gibbs free energy of proton absorption−desorption, responsible for improved HER activities. The Tafel plots obtained from the LSV polarization curves provided valuable insights into the electrochemical water splitting and the properties of the electrocatalyst. The lower Tafel plot indicates a fast increase in the current density relative to the rapid electrochemical water splitting and faster HER kinetics. The appropriate Tafel slopes for the $Bi_xTi_yO_z$/MOF-In_2S_3/$CdIn_2S4$/NiF, MOF-In_2S_3/NiF, $Bi_xTi_yO_z$/MOF-In_2S_3/NiF, and MOF-In_2S_3/$CdIn_2S_4$/NiF electrodes for the hydrogen evolution reaction are 106.0, 141.0, 123.0, and 237 mV dec^{-1}, respectively (Figure 8c). However, the lowest Tafel slope is obtained for the $Bi_xTi_yO_z$/MOF-In_2S_3/$CdIn_2S_4$/NiF electrocatalyst because of the synergetic effect of the composite electrocatalyst. Therefore, the $Bi_xTi_yO_z$/MOF-In_2S_3/$CdIn_2S_4$/NiF composite enhanced the electrocatalytic HER and reaction kinetics performance. The chronopotentiometry analysis performed at a current density of 10 mA cm^{-2} in Figure 8d exhibited the excellent efficiency of the electrocatalyst without any significant loss even after 45000 s of the test. Furthermore, the long-term stability of the as-fabricated catalyst under continuous HER conditions is the most important criterion for potential applications. Therefore, the long-term stability of the efficient $Bi_xTi_yO_z$ /MOF-In_2S_3/$CdIn_2S_4$/NiF composite catalyst was tested for 1000 CV cycles in the same 1 M KOH electrolyte solution. The initial and 1000-cycle LSV curves for the $Bi_xTi_yO_z$/MOF-In_2S_3/$CdIn_2S_4$/NiF catalyst are shown in Figure S5. The small overpotential range at the same low current density (10 mA/cm^{-1}) indicates the excellent electrochemical stability and durability of the $Bi_xTi_yO_z$/MOF-In_2S_3/$CdIn_2S_4$/NiF composite catalyst in terms of efficient HER activity.

TC degradation and Its Mechanism under Solar Light and Literature Comparison. TC is the most fundamental chemical in the TC family and has been utilized extensively throughout human history. When TC usage becomes excessive, this may also result in major health issues. Additionally, it is difficult to eliminate or downgrade the surplus TC. The degradation of TC was conducted under solar

https://doi.org/10.1021/acs.langmuir.3c02031
Langmuir 2023, 39, 15055−15066

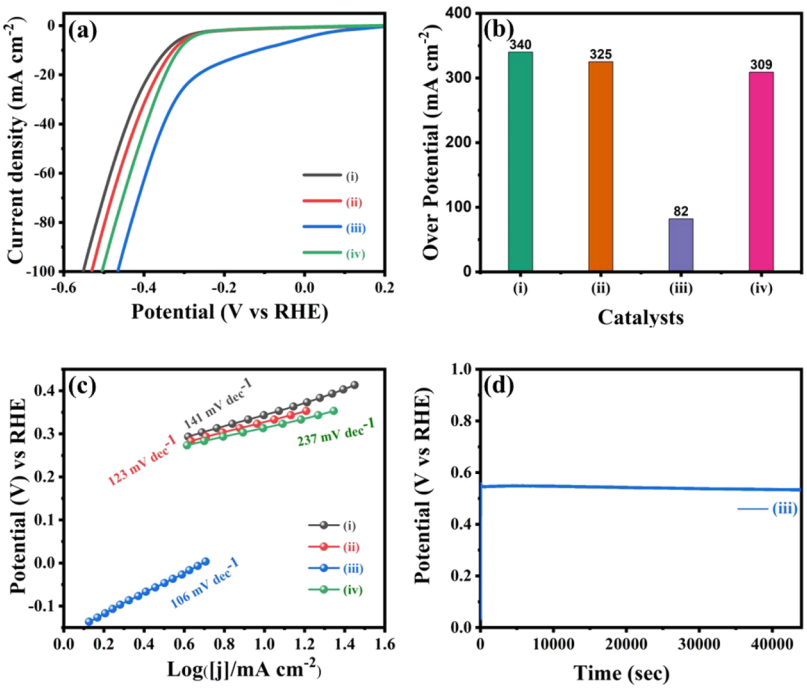

Figure 8. (a) Linear sweep voltammetry (LSV) curves, (b) overpotential, (c) Tafel polarization curves, (d) chronopotentiometric curves for 12 h, of the electrodes in 1.0 M KOH solution at a 10 mV s^{-1} scan rate; (i) MOF-In_2S_3, (ii) $Bi_xTi_yO_z$/MOF-In_2S_3, (iii) $Bi_xTi_yO_z$/MOF-In_2S_3/$CdIn_2S_4$, and (iv) MOF-In_2S_3/$CdIn_2S_4$.

light (direct sunlight) to verify the activity of the synthesized materials. The findings are shown in Figure S6a,b, which unmistakably demonstrates that as the irradiation time increases, the degradation of TC is likewise increased with catalysts. When $Bi_xTi_yO_z$ was used for TC degradation under solar light, the time of irradiation increased, and the percentage of degradation also increased to 62.5% up to 120 min irradiation; with the further increase in degradation time, there was no enhancement in the degradation efficiency up to 240 min. $Bi_xTi_yO_z$/MOF-In_2S_3 and $Bi_xTi_yO_z$/MOF-In_2S_3/$CdIn_2S_4$ were used for the degradation, and the TC concentration was decreased with respect to time and showed 66.4 and 64.1% of degradation, respectively, at 240 min. Under the same conditions, MOF-In_2S_3 and MOF-In_2S_3/$CdIn_2S_4$ showed 25.9 and 37.4% degradation, respectively. The corresponding kinetics data is provided in Figure S6c. The *pseudo*-first-order kinetics values for $Bi_xTi_yO_z$, MOF-In_2S_3, $Bi_xTi_yO_z$/MOF-In_2S_3, $Bi_xTi_yO_z$/MOF-In_2S_3/$CdIn_2S_4$, and MOF-In_2S_3/$CdIn_2S_4$ are 0.00385, 0.00119, 0.00447, 0.00415, and 0.00175 min^{-1}, respectively.

Based on the energy levels of these components,[63,64] an appropriate process for the development of heterostructure among MOF-In_2S_3, $Bi_xTi_yO_z$, and $CdIn_2S_4$ is provided and the possible TC degradation mechanism under solar light is proposed (Scheme S1). Because MOF-In_2S_3 had a CB position that is more negative than that of $Bi_xTi_yO_z$, the excited electrons would go from MOF-In_2S_3 to $Bi_xTi_yO_z$. It was anticipated that h^+ in the VB of $CdIn_2S_4$ and the accumulated e^- in the CB of $Bi_xTi_yO_z$ would combine, separating the e^- in the CB of $CdIn_2S_4$ and the h^+ in the VB of $Bi_xTi_yO_z$ and improving charge separation efficiency. Highly reactive oxygen species (ROS) are formed when holes and electrons react with water and dissolved oxygen. Both species are quite effective at degrading TC. Table S2 lists the literature comparison with Bi based/modified photocatalysts for TC degradation. The $Bi_xTi_yO_z$/MOF-In_2S_3/$CdIn_2S_4$ photocatalyst efficiently degrades the TC under direct solar light despite the different optimization techniques.

CONCLUSIONS

For the first time, we use a step-by-step process to design and produce Bi_2O_3/bismuth titanates modified with the MOF-In_2S_3/$CdIn_2S_4$ materials. The precise structural elucidation and phase development of mixed composite phases were thoroughly investigated. From the XRD, for the specimen, $Bi_xTi_yO_z$ showed the presence of a majority phase bismuth oxide (Bi_2O_3), with a monoclinic structure and *P*21/*c* SGS along with two different bismuth titanates $Bi_{12}TiO_{20}$ and the $Bi_4Ti_3O_{12}$. Finally, the other two specimens were developed based on a mixture of $Bi_xTi_yO_z$ and MOF-In_2S_3 (specimen $Bi_xTi_yO_z$/MOF-In_2S_3) and the mixture of $Bi_xTi_yO_z$ and MOF-In_2S_3/$CdIn_2S_4$ (specimen $Bi_xTi_yO_z$/MOF-In_2S_3/$CdIn_2S_4$). The PL intensity of the $Bi_xTi_yO_z$/MOF-In_2S_3/$CdIn_2S_4$ specimen is low compared with those of other components. The TEM study was carried out on the $Bi_xTi_yO_z$/MOF-In_2S_3/$CdIn_2S_4$ specimen, and it confirmed that this composition contains a mixture of the specimens $Bi_xTi_yO_z$ and MOF-In_2S_3/$CdIn_2S_4$. Thus, the introduction of Cd in $Bi_xTi_yO_z$/MOF-In_2S_3/$CdIn_2S_4$ caused the transformation of some In_2S_3 by In_2O_3 because of the excess amount of S required, and the remaining excess In^{3+} cations reacted with oxygen to form nanoembedded particles of In_2O_3; this was confirmed by HRTEM measurements of the $Bi_xTi_yO_z$/MOF-In_2S_3 specimen. From XPS, $CdIn_2S_4$ peaks are located at lower binning energies due to the presence of Ti atoms. The HER efficiency improved when $Bi_xTi_yO_z$ was incorporated into $CdIn_2S_4$/NiF. Moreover, the synergistic coupling effect of the electron transfer lowers the Gibbs free energy of proton absorption−desorption and is responsible for improved HER activities. The appropriate Tafel slopes for the $Bi_xTi_yO_z$/MOF-In_2S_3/$CdIn_2S_4$/NiF, MOF-

https://doi.org/10.1021/acs.langmuir.3c02031
Langmuir 2023, 39, 15055−15066

In_2S_3/NiF, $Bi_xTi_yO_z$/MOF-In_2S_3/NiF, and MOF-In_2S_3/$CdIn_2S_4$/NiF electrodes for the hydrogen evolution reaction are 106.0, 141.0, 123.0, and 237 mV dec^{-1}, respectively. The prepared composites were effectively utilized for TC degradation under solar light. Improved electrocatalytic activity of the material and photocatalytic activity under direct sunlight is favorable in the development of catalytic support for energy and environmental applications.

■ ASSOCIATED CONTENT

Supporting Information

The Supporting Information is available free of charge at https://pubs.acs.org/doi/10.1021/acs.langmuir.3c02031.

FE-SEM images of $Bi_xTi_yO_z$, MOF-In_2S_3, and $Bi_xTi_yO_z$/MOF-In_2S_3/$CdIn_2S_4$, FE-SEM images of for $Bi_xTi_yO_z$/MOF-In_2S_3, and MOF-In_2S_3/$CdIn_2S_4$, mapping STEM images for the $Bi_xTi_yO_z$/MOF-In_2S_3/$CdIn_2S_4$ material, polarization curves of the efficient $Bi_xTi_yO_z$/MOF-In_2S_3/$CdIn_2S_4$/NiF for the first and 1000th cycles, photodegradability of TC under direct solar light, mechanism of TC degradation by $Bi_xTi_yO_z$/MOF-In_2S_3/$CdIn_2S_4$ under solar light, surface properties of the $Bi_xTi_yO_z$ and $Bi_xTi_yO_z$/MOF-In_2S_3/$CdIn_2S_4$, and comparison of TC degradation efficiency (PDF)

■ AUTHOR INFORMATION

Corresponding Authors

Krishnakumar Balu − *Departamento de Ingeniería y Ciencia de los Materiales y del Transporte, E.T.S. de Ingenieros, Universidad de Sevilla, 41092 Sevilla, Spain; Department of Chemistry, Saveetha School of Engineering, Saveetha Institute of Medical and Technical Sciences, Saveetha University, Chennai, Tamil Nadu 602105, India;* orcid.org/0000-0003-0957-4978; Email: kbalu@us.es

Ernesto Chicardi − *Departamento de Ingeniería y Ciencia de los Materiales y del Transporte, E.T.S. de Ingenieros, Universidad de Sevilla, 41092 Sevilla, Spain;* orcid.org/0000-0002-6481-0438; Email: echicardi@us.es

Young-Ho Ahn − *Environmental Science and Engineering Laboratory, Department of Civil Engineering, Yeungnam University, Gyeongsan 38541, Republic of Korea;* orcid.org/0000-0002-8301-5886; Email: yhahn@ynu.ac.kr

Authors

Balakrishna Avula − *Department of Chemistry, Rajeev Gandhi Memorial College of Engineering and Technology (Autonomous), Nandyal, Andhra Pradesh 518501, India;* orcid.org/0000-0003-2866-4995

Mani Durai − *Environmental Science and Engineering Laboratory, Department of Civil Engineering, Yeungnam University, Gyeongsan 38541, Republic of Korea;* orcid.org/0000-0001-8871-4128

Sakthivel Kumaravel − *Department of Environmental Engineering, Korea Maritime and Ocean University, Busan 49112, Republic of Korea;* orcid.org/0000-0003-2426-5962

Ranier Sepúlveda − *Departamento de Ingeniería y Ciencia de los Materiales y del Transporte, E.T.S. de Ingenieros, Universidad de Sevilla, 41092 Sevilla, Spain;* orcid.org/0000-0002-7195-8131

Elangovan Erusappan − *Department of Applied Science and Technology, Anna University, Chennai, Tamil Nadu 600025, India;* orcid.org/0000-0001-7296-3963

Imran Hasan − *Department of Chemistry, College of Science, King Saud University, Riyadh 11451, Saudi Arabia;* orcid.org/0000-0002-5661-0655

Complete contact information is available at: https://pubs.acs.org/10.1021/acs.langmuir.3c02031

Author Contributions

[¶]K.B. and M.D. are equally contributed to this work.

Notes

The authors declare no competing financial interest.

■ ACKNOWLEDGMENTS

The authors extend their thanks to the Researchers Supporting Project (ref. RSPD2023R670), King Saud University, Riyadh, Saudi Arabia. This Research was supported by the Basic Science Research Program through the National Research Foundation of Korea funded by the Ministry of Education (2020R1l1A305481611). Dr. Krishnakumar Balu would like to thank the Ministry of Universities and the Recovery, Transformation and Resilience Plan from the Spanish government for the "María Zambrano grant 2021" by the European Union - NextGenerationEU.

■ REFERENCES

(1) Bao, Z.; Zhao, J.; Zhang, S.; Ding, L.; Peng, X.; Wang, G.; Zhao, Z.; Zhong, X.; Yao, Z.; Wang, J. Synergistic effect of doped nitrogen and oxygen containing functional groups on electrochemical synthesis of hydrogen peroxide. *J. Mater. Chem. A* **2022**, *10*, 4749−4757.

(2) Jiao, S.; Fu, X.; Wang, S.; Zhao, Y. Perfecting electrocatalysts via imperfections: towards the large-scale deployment of water electrolysis technology. *Energy Environ. Sci.* **2021**, *14*, 1722−1770.

(3) Wu, Z.; Wang, J.; Xia, K.; Lei, W.; Liu, X.; Wang, D. MoS_2-MoP heterostructured nanosheets on polymer-derived carbon as an electrocatalyst for hydrogen evolution reaction. *J. Mater. Chem. A* **2018**, *6*, 616−622.

(4) Yu, M.; Ding, B.; Wu, J.; Zheng, S.; Qian, X.; Zhang, L.; Zheng, S.; Mao, L.; Zhang, J. Novel incomplete phase transition from α-Bi_2O_3 to γ-Bi_2O_3 constructing dual interfaces contacts with $BaTiO_3$ for highly efficient degradation of antibiotics. *Chem. Eng. J.* **2023**, *464*, No. 142586.

(5) Mou, Y.; Wu, X.; Qin, C.; Chen, J.; Zhao, Y.; Jiang, L.; Zhang, C.; Yuan, X.; Huixiang Ang, E.; Wang, H. Linkage Microenvironment of Azoles-Related Covalent Organic Frameworks Precisely Regulates Photocatalytic Generation of Hydrogen Peroxide. *Angew. Chem., Int. Ed.* **2023**, *62*, No. e202309480.

(6) Wang, H.; Wu, Y.; Feng, M.; Tu, W.; Xiao, T.; Xiong, T.; Ang, H.; Yuan, X.; Chew, J. W. Visible-light-driven removal of tetracycline antibiotics and reclamation of hydrogen energy from natural water matrices and wastewater by polymeric carbon nitride foam. *Water Res.* **2018**, *144*, 215−225.

(7) Yu, W.; Gao, Y.; Chen, Z.; Zhao, Y.; Wu, Z.; Wang, L. Strategies on improving the electrocatalytic hydrogen evolution performances of metal phosphides. *Chin. J. Catal.* **2021**, *42*, 1876−1902.

(8) Chen, J.; Qin, C.; Mou, Y.; Cao, Y.; Chen, H.; Yuan, X.; Wang, H. Linker regulation of iron-based MOFs for highly effective Fenton-like degradation of refractory organic contaminants. *Chem. Eng. J.* **2023**, *459*, No. 141588.

(9) Tang, T.; Wang, Z.; Guan, J. review of defect engineering in two-dimensional materials for electrocatalytic hydrogen evolution reaction. *Chin. J. Catal.* **2022**, *43*, 636−678.

(10) Zhang, D.; Miao, H.; Wu, X.; Wang, Z.; Zhao, H.; Shi, Y.; Chen, X.; Xiao, Z.; Lai, J.; Wang, L. Scalable synthesis of ultra-small

Ru_2P@Ru/CNT for efficient seawater splitting. *Chin. J. Catal.* **2022**, *43*, 1148−1155.
(11) Cui, T.; Zhai, X.; Guo, L.; Chi, J. Q.; Zhang, Y.; Zhu, J.; Sun, X.; Wang, L. Controllable synthesis of a self-assembled ultralow Ru, Ni-doped Fe_2O_3 lily as a bifunctional electrocatalyst for large-current-density alkaline seawater electrolysis. *Chin. J. Catal.* **2022**, *43*, 2202−2211.
(12) Liu, Y.; Wang, H.; Yuan, X.; Wu, Y.; Wang, H.; Tan, Y. Z.; Chew, J. W. Roles of sulfur-edge sites, metal-edge sites, terrace sites, and defects in metal sulfides for photocatalysis. *Chem. Catalysis* **2021**, *1*, 44−68.
(13) Feng, X.; Zou, H.; Zheng, R.; Wei, W.; Wang, R.; Zou, W.; Lim, G.; Hong, J.; Duan, L.; Chen, H. Bi_2O_3/BiO_2 Nanoheterojunction for Highly Efficient Electrocatalytic CO_2 Reduction to Formate. *Nano Lett.* **2022**, *22*, 1656−1664.
(14) Ying, H.; Bi, J.; Xu, H.; Wu, G.; Wu, X.; Hao, J.; Li, Z. Mn-Doped Bi_2O_3 Nanosheets from a Deep Eutectic Solvent toward Enhanced Electrocatalytic N_2 Reduction. *ACS Sustainable Chem. Eng.* **2022**, *10*, 6766−6774.
(15) Zhang, N.; Wu, R.; Zhang, Y.; Yue, J.; Jing, H.; Wei, S.; Ouyang, F. CuS as bifunctional catalyst for enhancing photocatalytic degradation efficiency of $Bi_4Ti_3O_{12}$. *Opt. Mater.* **2023**, *138*, No. 113700.
(16) Kallawar, G. A.; Barai, D. P.; Bhanvase, B. A. Bismuth titanate based photocatalysts for degradation of persistent organic compounds in wastewater: A comprehensive review on synthesis methods, performance as photocatalyst and challenges. *J. Clean. Prod.* **2021**, *318*, No. 128563.
(17) Sarkar, S.; Jana, R.; Vadlamani, H.; Ramani, S.; Mumbaraddi, D.; Peter, S. C. Facile Aqueous-Phase Synthesis of the $PtAu/Bi_2O_3$ Hybrid Catalyst for Efficient Electro-Oxidation of Ethanol. *ACS Appl. Mater. Interfaces* **2017**, *9*, 15373−15382.
(18) Wang, Q.; Yang, G.; Fu, Y.; Li, N.; Hao, D.; Ma, S. Nanospace Engineering of Metal-Organic Frameworks for Heterogeneous Catalysis. *ChemNanoMat* **2022**, *8*, No. e202100396.
(19) You, W. F.; Xu, X.; Cao, A. H.; Tao, Z. J.; Kang, L. T. Synthesis of Axially Coordinated Cobalt Porphyrin/graphene Oxide Nanocomposite for Enhanced Electrocatalytic CO_2 Reduction to CO. *Chin. J. Struct. Chem.* **2022**, *41*, 2203001−2203011.
(20) Zhong, Y.; Wu, C.; Feng, Y.; Chen, D.; Wang, Y.; Hao, D.; Ding, H. Enriched surface oxygen vacancies of BiOCl boosting efficient charge separation, whole visible-light absorption, and photo to thermal conversion. *Appl. Surf. Sci.* **2022**, *585*, No. 152656.
(21) Hao, D.; Wei, Y.; Mao, L.; Bai, X.; Liu, Y.; Xu, B.; Wei, W.; Ni, B. J. Boosted selective catalytic nitrate reduction to ammonia on carbon/bismuth/bismuth oxide photocatalysts. *J. Clean. Prod.* **2022**, *331*, No. 129975.
(22) Hao, D.; Liu, Y.; Gao, S.; Arandiyan, H.; Bai, X.; Kong, Q.; Wei, W.; Shen, P. K.; Ni, B. J. Emerging artificial nitrogen cycle processes through novel electrochemical and photochemical synthesis. *Mater. Today* **2021**, *46*, 212−233.
(23) Mahadadalkar, M. A.; Kale, S. B.; Kalubarme, R. S.; Bhirud, A. P.; Ambekar, J. D.; Gosavi, S. W.; Kulkarni, M. V.; Park, C. J.; Kale, B. B. Architecture of the $CdIn_2S_4$/graphene nano-heterostructure for solar hydrogen production and anode for lithium ion battery. *RSC Adv.* **2016**, *6*, 34724−34736.
(24) Fan, L.; Guo, R. Fabrication of Novel $CdIn_2S_4$ Hollow Spheres via a Facile Hydrothermal Process. *J. Phys. Chem. C* **2008**, *112*, 10700−10706.
(25) Chen, Y.; Huang, R.; Chen, D.; Wang, Y.; Liu, W.; Li, X.; Li, Z. Exploring the Different Photocatalytic Performance for Dye Degradations over Hexagonal $ZnIn_2S_4$ Microspheres and Cubic $ZnIn_2S_4$ Nanoparticles. *ACS Appl. Mater. Interfaces* **2012**, *4*, 2273−2279.
(26) Xie, Z.; Liu, G.; Xie, L.; Wu, P.; Liu, H.; Wang, J.; Xie, Y.; Chen, J.; Lu, C. Z. Promoting photocatalytic H_2 evolution through interfacial charge separation on the direct Z-scheme $ZnIn_2S_4/ZrO_2$ heterojunction. *Int. J. Hydrogen Energy* **2023**, *48*, 32782−32796, DOI: 10.1016/j.ijhydene.2023.05.038.
(27) Wang, Y.; Ye, J.; Hu, B.; Xie, Y.; Ling, Y.; Wang, Z.; Chen, Y. NiO co-catalyst modification $ZnIn_2S_4$ driving efficient hydrogen generation under visible light. *Sep. Purif. Technol.* **2023**, *320*, No. 124096.
(28) Chen, W.; Bovin, J. O.; Joly, A. G.; Wang, S.; Su, F.; Li, G. Full-Color Emission from In_2S_3 and In_2S_3: Eu^{3+} Nanoparticles. *J. Phys. Chem. B* **2004**, *108*, 11927−11934.
(29) Mishra, S. R.; Gadore, V. Novel 3D sphere-like β-In_2S_3/Biochar nanoflowers for remediation of dyes in single and binary systems and interpretation using statistical physical modelling. *Environ. Nanotechnol. Monit. Manag.* **2023**, *20*, No. 100807.
(30) Tapia, C.; Zacarias, S.; Pereira, I. A. C.; Conesa, J. C.; Pita, M.; Lacey, A. L. D. In Situ Determination of Photobioproduction of H_2 by In_2S_3-[NiFeSe] Hydrogenase from Desulfovibrio vulgaris Hildenborough Using Only Visible Light. *ACS Catal.* **2016**, *6*, 5691−5698.
(31) Guo, S.; Chen, X.; Hu, F.; Zhang, Q.; Liu, L. Ultralong In_2S_3 Nanotubes on Graphene Substrate with Enhanced Electrocatalytic Activity. *ACS Appl. Mater. Interfaces* **2015**, *7*, 20164−20169.
(32) Wang, L.; Xia, L.; Wu, Y.; Tian, Y. Zr-Doped β-In_2S_3 Ultrathin Nanoflakes as Photoanodes: Enhanced Visible-Light-Driven Photoelectrochemical Water Splitting. *ACS Sustainable Chem. Eng.* **2016**, *4*, 2606−2614.
(33) Chen, X.; Li, L.; Zhang, W.; Li, Y.; Song, Q.; Dong, L. Fabricate Globular Flower-like $CuS/CdIn_2S_4/ZnIn_2S_4$ with High Visible Light Response via Microwave-assisted One-step Method and Its Multi-pathway Photoelectron Migration Properties for Hydrogen Evolution and Pollutant Degradation. *ACS Sustainable Chem. Eng.* **2016**, *4*, 6680−6688.
(34) Zhou, Y.; Zhao, X.; Liang, Q.; Zhou, M.; Li, X.; Xu, S.; Li, Z. In situ growth of $CdIn_2S_4$ on NH_2-MIL-125 as efficient photocatalysts for H_2 production under visible-light irradiation. *J. Phys. Chem. Solids* **2023**, *173*, No. 111096.
(35) Oropeza, F. E.; Villar-Garcia, I. J.; Palgrave, R. G.; Payne, D. J. A solution chemistry approach to epitaxial growth and stabilisation of $Bi_2Ti_2O_7$ films. *J. Mater. Chem. A* **2014**, *2*, 18241−18245.
(36) Cheng, J.; Hou, H.; Takeda, O.; Guo, M. X.; Zhu, H. A unique Z-scheme 2D/2D nanosheet heterojunction design to harness charge transfer for photocatalysis. *J. Mater. Chem. A* **2015**, *3*, 11006−11013.
(37) Grao, M.; Redfern, J.; Kelly, P.; Ratova, M. Photocatalytic degradation of contaminants of emerging concern using a low-cost and efficient black bismuth titanate-based water treatment reactor. *J. Water Process. Eng.* **2022**, *45*, No. 102525.
(38) Xia, A.; Tan, G.; Ren, H. Microwave hydrothermal synthesis of a new bismuth titanate compound. *Mater. Today Commun.* **2016**, *8*, 134−138.
(39) Kallawar, G. A.; Barai, D. P.; Bhanvase, B. A. Bismuth titanate based photocatalysts for degradation of persistent organic compounds in wastewater: A comprehensive review on synthesis methods, performance as photocatalyst and challenges. *J. Clean. Prod.* **2021**, *318*, No. 128563.
(40) Zhang, N.; Wu, R.; Zhang, Y.; Yue, J.; Jing, H.; Wei, S.; Ouyang, F. CuS as bifunctional catalyst for enhancing photocatalytic degradation efficiency of $Bi_4Ti_3O_{12}$. *Opt. Mater.* **2023**, *138*, No. 113700.
(41) Ren, Y.; Liu, X.; Li, H.; Wang, X.; Jing, X. Synthesis and visible light photocatalytic performance of $HC/BiOBr/Bi_{12}TiO_{20}$ microspheres. *Chem. Phys. Lett.* **2022**, *797*, No. 139584.
(42) Hou, J.; Cao, R.; Wang, Z.; Jiao, S.; Zhu, S. Chromium-doped bismuth titanate nanosheets as enhanced visible-light photocatalysts with a high percentage of reactive {110} facets. *J. Mater. Chem.* **2011**, *21*, 7296−7301.
(43) Yang, L.; Liu, X.; Yang, T.; Chen, Z.; Guo, J.; Zheng, L.; Xiao, X.; Zeng, G.; Luo, X.; Luo, S. Electrochemical recovery of total Cr by reduction alongside immobilization using an acethydrazide functionalized Fe/Ni-MIL-53 MOF electrode. *Resour. Conserv. Recycl.* **2023**, *191*, No. 106884.
(44) Nivetha, R.; Kollu, P.; Chandar, K.; Pitchaimuthu, S.; Jeongf, S. K.; Grace, A. N. Role of MIL-53(Fe)/hydrated−dehydrated MOF

catalyst for electrochemical hydrogen evolution reaction (HER) in alkaline medium and photocatalysis. *RSC Adv.* **2019**, *9*, 3215−3223.
(45) Zhang, P.; Yin, X.; Zhang, D.; Guo, P.; Liu, W.; Wang, R.; Zhang, Z.; Qiu, S. MOF templated to construct hierarchical $ZnIn_2S_4$-In_2S_3 hollow nanotube for enhancing photocatalytic performance. *Chem. Eng. J.* **2023**, *458*, No. 141394.
(46) Xu, J.; Li, Q.; Sui, D.; Jiang, W.; Liu, F.; Gu, X.; Zhao, Y.; Ying, P.; Mao, L.; Cai, X.; Zhang, J. In Situ Photodeposition of Cobalt Phosphate (CoHxPOy) on $CdIn_2S_4$ Photocatalyst for Accelerated Hole Extraction and Improved Hydrogen Evolution. *Nanomaterials* **2023**, *13*, 420.
(47) Bariki, R.; Majhi, D.; Das, K.; Behera, A.; Mishra, B. G. Facile synthesis and photocatalytic efficacy of UiO-66/$CdIn_2S_4$ nanocomposites with flowerlike 3D-microspheres towards aqueous phase decontamination of triclosan and H_2 evolution. *Appl. Catal., B* **2020**, *270*, No. 118882.
(48) Ma, D.; Shi, J.; Zou, W. Y.; Fan, Z.; Shi, J.; Cheng, L.; Sun, D.; Wang, Z.; Niu, C. Multiple carrier-transfer pathways in a flower-like In_2S_3/$CdIn_2S_4$/In_2O_3 ternary heterostructure for enhanced photocatalytic hydrogen production. *Nanoscale* **2018**, *10*, 7860−7870.
(49) Jiang, R.; Mao, L.; Zhao, Y.; Zhang, J.; Cai, X.; Gu, X. Spatial carrier separation in cobalt phosphate deposited $ZnIn_2S_4$ nanosheets for efficient photocatalytic hydrogen evolution. *J. Colloid Interface Sci.* **2022**, *606*, 317−327.
(50) Chen, X.; Li, W.; Zhang, L.; Li, Y.; Song, Q.; Dong, L. Fabricate Globular Flower-like CuS/$CdIn_2S_4$/$ZnIn_2S_4$ with High Visible Light Response via Microwave-assisted One−step Method and Its Multi-pathway Photoelectron Migration Properties for Hydrogen Evolution and Pollutant Degradation. *ACS Sustainable Chem. Eng.* **2016**, *4* (12), 6680−6688.
(51) Singh, J.; Soni, R. K. Enhanced sunlight driven photocatalytic activity of In_2S_3 nanosheets functionalized MoS_2 nanoflowers heterostructures. *Sci. Rep.* **2021**, *11*, 15352.
(52) Cheng, Y.; Niu, H.; Chen, J.; Song, J.; Mao, C.; Zhang, S.; Chen, C.; Gao, Y. Highly Stable Hierarchical Flower-like β-In_2S_3 Assembled from 2D Nanosheets with high Adsorption-Photodecolorization Activities for the Treatment of Wastewater. *J. Nanopart. Res.* **2017**, *19*, 166.
(53) Rösler, C.; Fische, R. A. Metal-organic frameworks as hosts for nanoparticles. *Cryst. Eng. Comm* **2015**, *17*, 199−217.
(54) Divya, J.; Shivaramu, N. J.; Purcell, W.; Roos, W. D.; Swart, H. C. Multifunction applications of Bi_2O_3:Eu^{3+} nanophosphor for red light emission and photocatalytic activity. *Appl. Surf. Sci.* **2019**, *497*, No. 143748.
(55) Liu, Y.; Wang, C.; Ju, S.; Li, M.; Yuan, A.; Zhu, G. FeCo-based hybrid MOF derived active species for effective oxygen evolution. *Prog. Nat. Sci.: Mater. Int.* **2020**, *30*, 185−191.
(56) Zhang, Q.; Lei, Y.; Li, L.; Lei, J.; Hu, M.; Deng, T.; Zhang, Y.; Ma, P. Construction of the novel PMA@Bi-MOF catalyst for effective fatty acid esterification. *Sustain. Chem. Pharm.* **2023**, *33*, No. 101038.
(57) Liu, B.; Hu, X.; Li, X.; Li, Y.; Chen, C.; Lam, K. Preparation of ZnS@In_2S_3 Core@shell Composite for Enhanced Photocatalytic Degradation of Gaseous o-Dichlorobenzene under Visible Light. *Sci. Rep.* **2017**, *7*, 16396.
(58) Xiao, Y.; Peng, Z.; Zhang, S.; Jiang, Y.; Jing, X.; Yang, X.; Zhang, J.; Ni, L. Z-scheme $CdIn_2S_4$/BiOCl nanosheet face-to-face heterostructure: in-situ synthesis and enhanced interfacial charge transfer for high-efficient photocatalytic performance. *J. Mater. Sci.* **2019**, *54*, 9573−9590.
(59) Chen, Y.; Hu, Qi; Yu, M.; Gong, X.; Li, S.; Wang, S.; Yu, H.; Li, Z. In situ construction of a direct Z-scheme $CdIn_2S_4$/TiO_2 heterojunction for improving photocatalytic properties. *CrystEngComm* **2021**, *23*, 5070−5077.
(60) Biesinger, M. C.; Lau, L. W.M.; Gerson, A. R.; Smart, R. S.C. Resolving surface chemical states in XPS analysis of first row transition metals, oxides and hydroxides: Sc, Ti, V, Cu and Zn. *Appl. Surf. Sci.* **2010**, *257*, 887−898.
(61) Hou, D.; Hu, X.; Wen, Y.; Shan, B.; Hu, P.; Xiong, X.; Qiao, Y.; Huang, Y. Electrospun sillenite $Bi_{12}MO_{20}$ (M = Ti, Ge, Si) nanofibers: general synthesis, band structure, and photocatalytic activity. *Phys. Chem. Chem. Phys.* **2013**, *15*, 20698−20705.
(62) Ramanery, F. P.; Mansur, A. A. P.; Mansur, H. S.; Carvalho, S. M.; Fonseca, M. C. Biocompatible Fluorescent Core-Shell Nanoconjugates Based on Chitosan/Bi_2S_3 Quantum Dots. *Nanoscale Res. Lett.* **2016**, *11*, 187.
(63) Wang, S.; Guan, B. Y.; Lu, Y.; Lou, X. W. D. Formation of Hierarchical In_2S_3−$CdIn_2S_4$ Heterostructured Nanotubes for Efficient and Stable Visible Light CO_2 Reduction. *J. Am. Chem. Soc.* **2017**, *139*, 17305−17308.
(64) Abdul Hannan Zahid, A. H.; Han, Q. A review on the preparation, microstructure, and photocatalytic performance of Bi_2O_3 in polymorphs. *Nanoscale* **2021**, *13*, 17687−17724.

https://doi.org/10.1021/acs.langmuir.3c02031
Langmuir 2023, 39, 15055−15066